



# Dirac-vortex topological cavities

Xiaomei Gao<sup>1,2,6</sup>, Lechen Yang<sup>1,3,6</sup>, Hao Lin<sup>1,3</sup>, Lang Zhang<sup>1,2</sup>, Jiafang Li<sup>1</sup>, Fang Bo<sup>2</sup>, Zhong Wang<sup>4</sup> and Ling Lu<sup>1,5</sup> ✉

**Cavity design is crucial for single-mode semiconductor lasers such as the ubiquitous distributed feedback and vertical-cavity surface-emitting lasers. By recognizing that both of these optical resonators feature a single mid-gap mode localized at a topological defect in the one-dimensional lattice, we upgrade this topological cavity design concept into two dimensions using a honeycomb photonic crystal with a vortex Dirac gap by applying the generalized Kekulé modulations. We theoretically predict and experimentally show on a silicon-on-insulator platform that the Dirac-vortex cavities have scalable mode areas, arbitrary mode degeneracies, vector-beam vertical emission and compatibility with high-index substrates. Moreover, we demonstrate the unprecedentedly large free spectral range, which defies the universal inverse relation between resonance spacing and resonator size. We believe that our topological micro-resonator will be especially useful in applications where single-mode behaviour is required over a large area, such as the photonic-crystal surface-emitting laser.**

Single-mode diode lasers<sup>1</sup> are the standard light sources for numerous applications, in which the mode selectivity is provided by the semiconductor cavity with subwavelength features. In long-haul fibre networks, the distributed feedback (DFB) laser<sup>2</sup> (Fig. 1) of a uniform Bragg grating has two competing band-edge modes with the lowest group velocities and degenerate thresholds. Although the mode selection can be done by facet cleaving with a certain yield, a much stabler solution is to introduce a quarter-wavelength shift<sup>3,4</sup> so that a single mid-gap mode can lase first at the Bragg frequency where the grating feedback is the strongest. Such one-dimensional (1D) mid-gap design is also adopted for vertical-cavity surface-emitting lasers (VCSELs)<sup>1</sup> to select a single longitudinal mode, used in local communications, computer mice and face recognition. Advancing to two-dimensional (2D) periodicity<sup>5,6</sup>, the photonic-crystal surface-emitting laser (PCSEL) has recently been commercialized<sup>7</sup> for its broader area and higher brightness<sup>8,9</sup> than the 1D counterparts, while maintaining the single-mode operation. However, PCSELs again have at least two high-quality-factor (*Q*) band-edge modes competing for lasing. It is obviously important to have a 2D cavity of a single robust mid-gap mode, which has been lacking since the notion of 2D DFB was first introduced<sup>5</sup>.

In order to design the 2D mid-gap defect cavity, we first recognize that the mid-gap modes of both the phase-shifted DFB and VCSEL are in fact topological (details in Supplementary Part A) and are mathematically equivalent to the Shockley surface state<sup>10</sup>, Jackiw–Rebbi zero mode<sup>11</sup> and Su–Schrieffer–Heeger (SSH) edge state<sup>12</sup>. This topological view leads us to the Jackiw–Rossi zero modes in 2D Dirac equations<sup>13</sup> and the Hou–Chamon–Mudry (HCM) model in graphene<sup>14</sup>, which we realize in a honeycomb photonic crystal with a vortex gap—the Dirac-vortex cavity. So far, the topological photonic research<sup>15–17</sup> has focused on robust waveguiding, including topological lasers<sup>18–21</sup> in which the cavities are formed by wrapping around topological waveguides. Although the defect cavity has recently been found at the corner of the 2D bulk crystal due to high-order topology<sup>22–25</sup>, it requires precise edge cuttings and has limited scalability in size.

Our Dirac-vortex cavity offers both a single mid-gap mode and the largest free spectral range (FSR) among all known sizeable resonators—a property not shared by the 1D topological counterparts. A large FSR is important for stabler single-mode operation, a higher spontaneous emission factor and a wider spectral tuning range. The FSR of a Dirac-vortex cavity can be one to two orders of magnitude larger than that of the conventional cavities (details in Supplementary Part B), due to a completely different scaling law between the FSR and mode volume (*V*). For conventional cavities, such as the Fabry–Perot, whispering-gallery and photonic crystal band-edge cavities<sup>26</sup>, the FSR ( $\propto \frac{1}{V}$ ) is inversely proportional to the mode volume, so that the routine practice to widen the FSR is to shorten the cavity size. Being uniquely advantageous, the FSR ( $\propto \frac{1}{\sqrt{V}}$ ) of the Dirac-vortex cavity is inversely proportional to the square root of its mode volume. This remarkable feature comes from the construction of a single cavity mode at the middle of the Dirac spectrum where the optical density of states vanishes, so that the FSR is spectrally non-uniform and peaks at the Dirac frequency. This is in contrast to the constant photon density of states in other types of cavities, in which the FSR is spectrally uniform. Consequently, the Dirac-vortex cavity has an ideal single-mode behaviour over large areas<sup>27</sup>.

## Jackiw–Rossi zero modes

The Dirac-vortex cavity is a photonic realization of the zero-mode solutions to the Dirac equations with mass vortices, proposed by Jackiw and Rossi<sup>13</sup>. Equation (1) is the time-reversal invariant Dirac Hamiltonian containing all five anti-commuting terms, where  $k_i$  is the momentum and  $\sigma_i$  and  $\tau_i$  are both Pauli matrices. A non-zero mass term ( $m_i$ ) produces a gapped Dirac spectrum. Consistent terminology as the effective mass is used in semiconductor physics to describe the band curvature.

$$H(\mathbf{k}) = (\sigma_x k_x + \sigma_z k_y)\tau_z + m_1\tau_x + m_2\tau_y + m'\sigma_y\tau_z \quad (1)$$

From the eigen-solution  $E(\mathbf{k}) = \pm \sqrt{\sum_i (k_i^2 + m_i^2)}$ , the two momentum terms in equation (1) form four-by-four massless

<sup>1</sup>Institute of Physics, Chinese Academy of Sciences/Beijing National Laboratory for Condensed Matter Physics, Beijing, China. <sup>2</sup>MOE Key Laboratory of Weak-Light Nonlinear Photonics, TEDA Institute of Applied Physics and School of Physics, Nankai University, Tianjin, China. <sup>3</sup>School of Physical Sciences, University of Chinese Academy of Sciences, Beijing, China. <sup>4</sup>Institute for Advanced Study, Tsinghua University, Beijing, China. <sup>5</sup>Songshan Lake Materials Laboratory, Dongguan, China. <sup>6</sup>These authors contributed equally: Xiaomei Gao, Lechen Yang. ✉e-mail: [linglu@iphy.ac.cn](mailto:linglu@iphy.ac.cn)

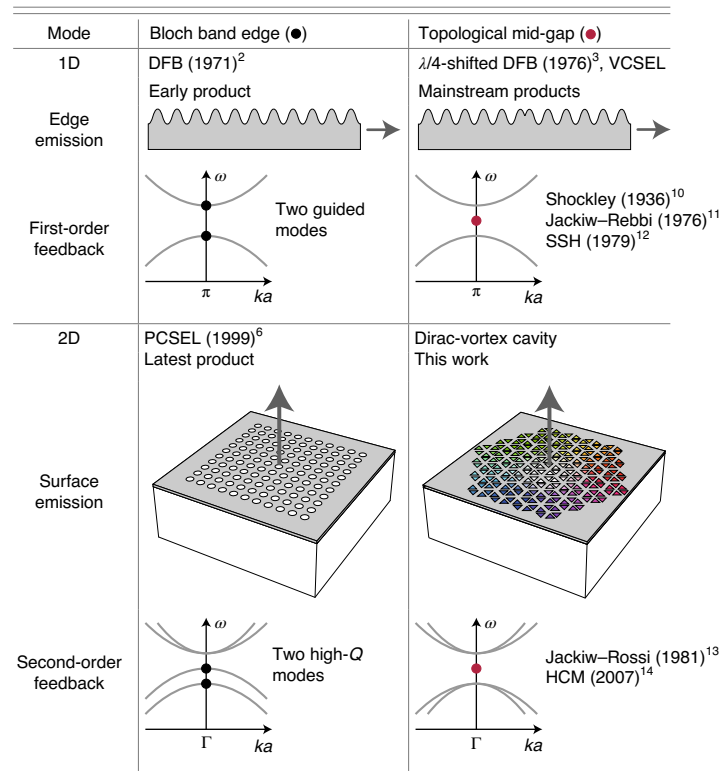


**Fig. 1 | Comparison of the Dirac-vortex cavity and the three types of commercialized semiconductor laser cavities for single-mode operation.** The cavities of uniform lattices, both 1D DFB and 2D PCSEL, have two competing high-Q band-edge modes. The cavities of topological defects, both the phase-shifted DFB and the Dirac-vortex cavities, have a single mid-gap mode. The years and references indicate when the device ideas and the corresponding topological models were first proposed.  $\omega$ , frequency;  $\lambda$ , wavelength;  $k$ , wavevector;  $a$ , lattice constant.

Dirac cones in two dimensions and the three mass terms represent three independent mathematical degrees of freedom that can gap the double Dirac cones. If the system has only two mass terms<sup>28</sup>, a vortex solution can form by spatially winding the mass terms in-plane. Fortunately, the third mass term  $m'$  vanishes when the dispersion spectrum is up-down symmetric with respect to the Dirac frequency. This protecting symmetry is the chiral symmetry  $S = \sigma_y \tau_z$  ( $SHS^{-1} = -H$ ) whose presence requires  $m' = 0$  (details in Supplementary Part C). Then the remaining two mass terms form a complex number ( $\mathbf{m} = m_1 + jm_2$ ) that can wind in-plane  $w$  times as  $\mathbf{m}(\mathbf{r}) \propto \exp[jw \arg(\mathbf{r})]$ , in which  $\mathbf{r}$  is the spatial coordinate and  $j^2 = -1$ . The  $w$  is the Dirac-mass winding number, the topological invariant of the vortex<sup>29</sup> belonging to the Altland–Zirnbauer symmetry class BDI ( $\mathbb{Z}$ ). The magnitude and sign of  $w$  determine the number and chirality of the mid-gap modes. We note that in a realistic photonic system at a non-zero frequency, the chiral symmetry is slightly broken and  $m'$  is not precisely zero. The resulting Dirac spectrum is not exactly up-down symmetric and the  $w$  topological modes are not rigorously degenerate in frequency.

### Honeycomb photonic crystal with generalized Kekulé modulations

The realization of Jackiw–Rossi modes in condensed matter systems was first proposed by Hou, Chamon and Mudry<sup>14</sup> in a Kekulé-textured graphene<sup>14</sup>. Although creating a vortex potential at the atomic level is a tall order, the realizations in designer photonic<sup>30–32</sup> and phononic lattices<sup>33,34</sup> have clear advantages. In this section, we construct the Jackiw–Rossi modes in an air-clad photonic-crystal membrane, and focus on the transverse-electric-like (TE-like) modes (electric field in-plane) that are favoured for most applications.

The starting point is a hexagon supercell consisting of three honeycomb primitive cells (Fig. 2a). This supercell folds the two Dirac points from the Brillouin-zone boundary ( $\pm K$  points below the light cone) to the zone centre ( $\Gamma$  point above the light cone), forming a four-by-four double Dirac cone dispersion (Fig. 2b). The two honeycomb sublattices are coloured in black and grey, both representing air holes in the silicon membrane. The triangular hole shape, compared to the circular shape, improves the frequency isolation of the Dirac points<sup>35,36</sup>. In fact, the previous topological waveguide design<sup>37</sup> between two deformed honeycomb lattices, by expanding and shrinking, corresponds to two discrete phase values (0 and  $\pi$ ) of the Dirac gap (mass terms). By contrast, the topological cavity utilizes the complete  $2\pi$  vortex phase for in-plane photon confinement.

We apply a generalized Kekulé modulation<sup>14,30</sup> in the supercell to generate the  $2\pi$  vortex gap of the double Dirac cones. Shown in Fig. 2a, the three grey sublattice air holes are shifted from their original positions by the same amplitude  $m_0$  and correlated phase  $\phi_0$ . The key observation is the persistent gap opening for all  $2\pi$  values of  $\phi_0$  with non-zero  $m_0$ , while the gap closes at the vortex centre where  $m_0 = 0$ . As plotted in Fig. 2c, the vortex band gap has an angular periodicity of  $\pi/3$  due to the lattice symmetry, and the minimal gap size occurs at  $\phi_0 = 0$ . The gap size as a function of  $m_0$  is plotted in Fig. 2d. The  $2\pi$  vortex gap peaks at 6% and eventually closes for large  $m_0$  because the band at the M point drops. Since the modulation vector  $\mathbf{m} = m_0 e^{j\phi_0}$  has the same physical consequence as that of the complex Dirac mass  $\mathbf{m} = m_1 + jm_2$  in equation (1), we use the same symbol in this paper.

Since we have a library of supercells with a vortex band gap whose phase continuously varies by  $2\pi$ , the cavity formation is a

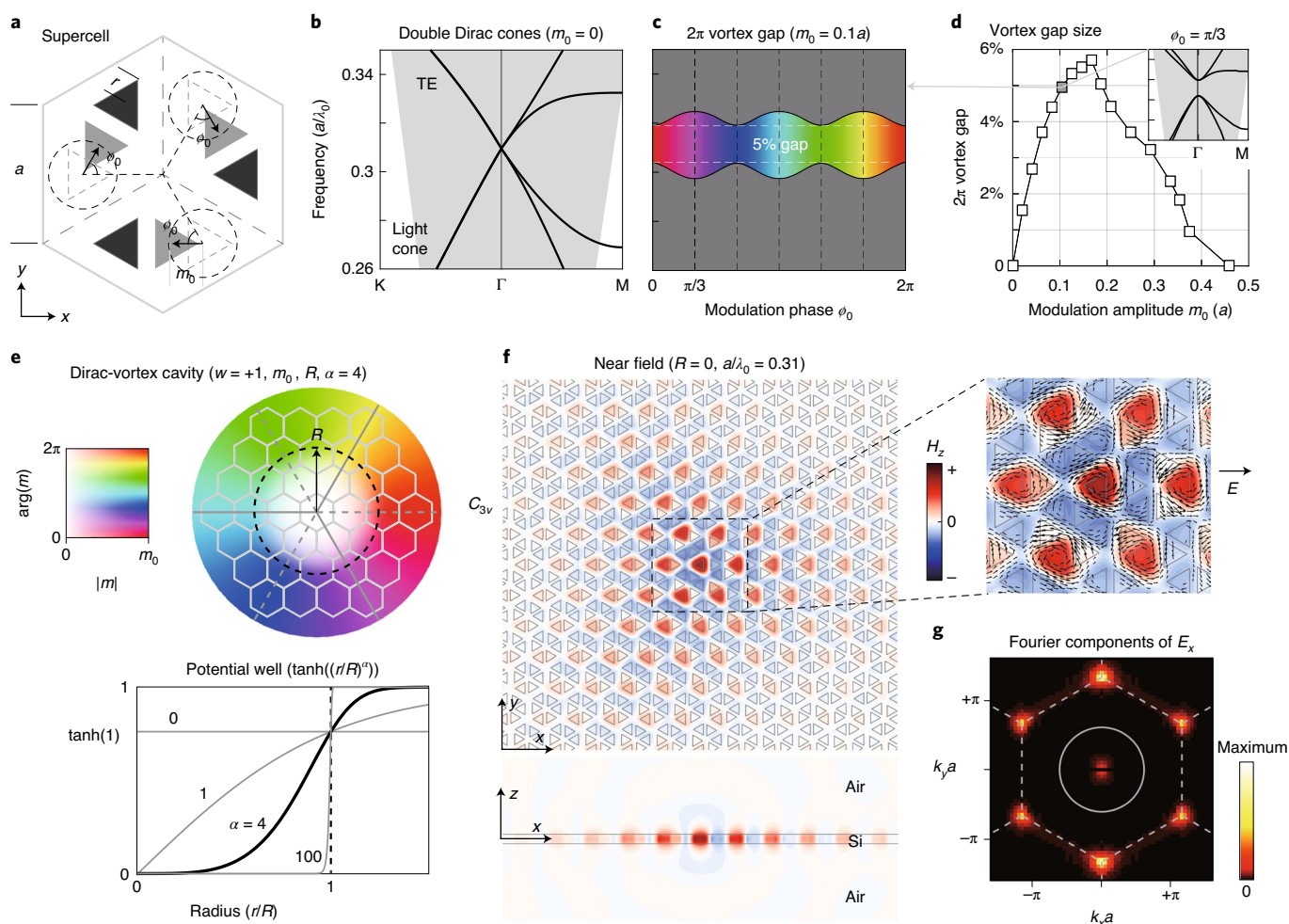


**Fig. 2 | Design of the photonic-crystal Dirac-vortex cavity in an air-clad silicon membrane (0.46a thick,  $n = 3.4$ ) by three-dimensional (3D) simulations for the TE-like modes. **a**, Honeycomb supercell of the generalized Kekulé modulation, in which the triangular air holes have  $r = 0.32a$ . **b**, Double Dirac cone band structure of the unperturbed supercell inside the shaded light cone. **c**, Band gap opens for  $2\pi$  angle of  $\phi_0$  and non-zero  $m_0$ , where the cyclic colour map represents the phase of the modulation. **d**, Band gap size as a function of  $m_0$ . **e**, Illustration of the Dirac-vortex cavity and the potential-well function. **f**, Near fields of the topological mode with  $m_0 = 0.1a$ ,  $Q = 317$  and  $V = 4.0(\lambda_0/n)^3$ , where  $\lambda_0$  is the vacuum wavelength. **g**, The magnitudes of the Fourier-transformed fields  $|\text{FT}(E_x)|$  in the momentum space, where the Brillouin-zone boundary of the primitive cell and the light cone is outlined.**

matter of arranging these supercells angularly around a cavity centre ( $\mathbf{r}_0$ ), as illustrated in Fig. 2e. Since the original honeycomb lattice ( $m_0 = 0$ ) has  $C_6$  symmetry, the vortex cavity ( $m_0 \neq 0$ ) can always remain  $C_{3v}$  symmetric if a  $w$ -dependent vortex centre ( $\mathbf{r}_0$ ) is chosen (illustrated in Supplementary Part D). A highly symmetric ( $D_{3h}$ ) design reduces the computation domain and eases the analysis through group theory.

The topological mid-gap mode is plotted in Fig. 2f. The Fourier components of the mode, in Fig. 2g, reveal its momentum distribution in relation to the light cone. Once the K points move inside the light cone of the substrate, the cavity resonance is no longer well defined (see the subsequent section Substrate compatibility).

### Cavity parameters

The design of the Dirac-vortex cavity is equivalent to the choice of spatial function for the vortex modulation  $\mathbf{m}(\mathbf{r} - \mathbf{r}_0)$ . Without loss of generality, we choose the following form of equation (2):

$$\mathbf{m}(\mathbf{r} - \mathbf{r}_0; w, m_0, R, \alpha) = m_0 \tanh\left(\left|\frac{\mathbf{r} - \mathbf{r}_0}{R}\right|^\alpha\right) e^{j[\phi_0 - w \arg(\mathbf{r} - \mathbf{r}_0)]} \quad (2)$$

The potential-well function  $\tanh(x^\alpha)|_{x \rightarrow +\infty} = +1$  and  $\tanh(x^\alpha)|_{x \rightarrow 0} = x^\alpha$ , interpreting from the central zero modulation

amplitude  $|\mathbf{m}(\mathbf{r} - \mathbf{r}_0)| = 0$  to the boundary maximum modulation amplitude  $|\mathbf{m}(\mathbf{r} \gg \mathbf{r}_0)| = m_0$ . The cavity is determined by four parameters ( $w, m_0, R$  and  $\alpha$ ), illustrated in Fig. 2e.

The first parameter  $w$  is the winding number of the vortex. The magnitude  $|w|$  determines the number (degeneracy) of mid-gap modes and the mode area increases with  $w$ , similar to the topological fibre case<sup>28</sup>. The sign of  $w$  is the mode chirality, determining which sublattice the field distribution will occur on. The topological mode populates only one of the honeycomb sublattices and, when  $w$  changes sign, populates the other (details in Supplementary Part E). In Fig. 2f, both the magnetic ( $H_z$ ) and electric ( $E_{x,y}$ ) fields peak only at the triangles pointing to the left.

The second parameter  $m_0$  is the maximum modulation amplitude, the maximum shift of the honeycomb sublattice in Fig. 2a, determining the depth of the potential well in Fig. 2e;  $m_0$  is also the strength of the radiative coupling that couples the two (originally guided) Dirac points into the light cone (radiation continuum). Therefore the cavity  $Q$  increases as  $m_0$  decreases.

The third parameter  $R$ , the vortex radius, should not be mistaken as the size of the whole cavity outside of which the photonic-crystal pattern ends. In fact, we pad at least fifty extra periods outside the vortex radius  $R$  to ensure sufficient mode confinement. The  $R$  can

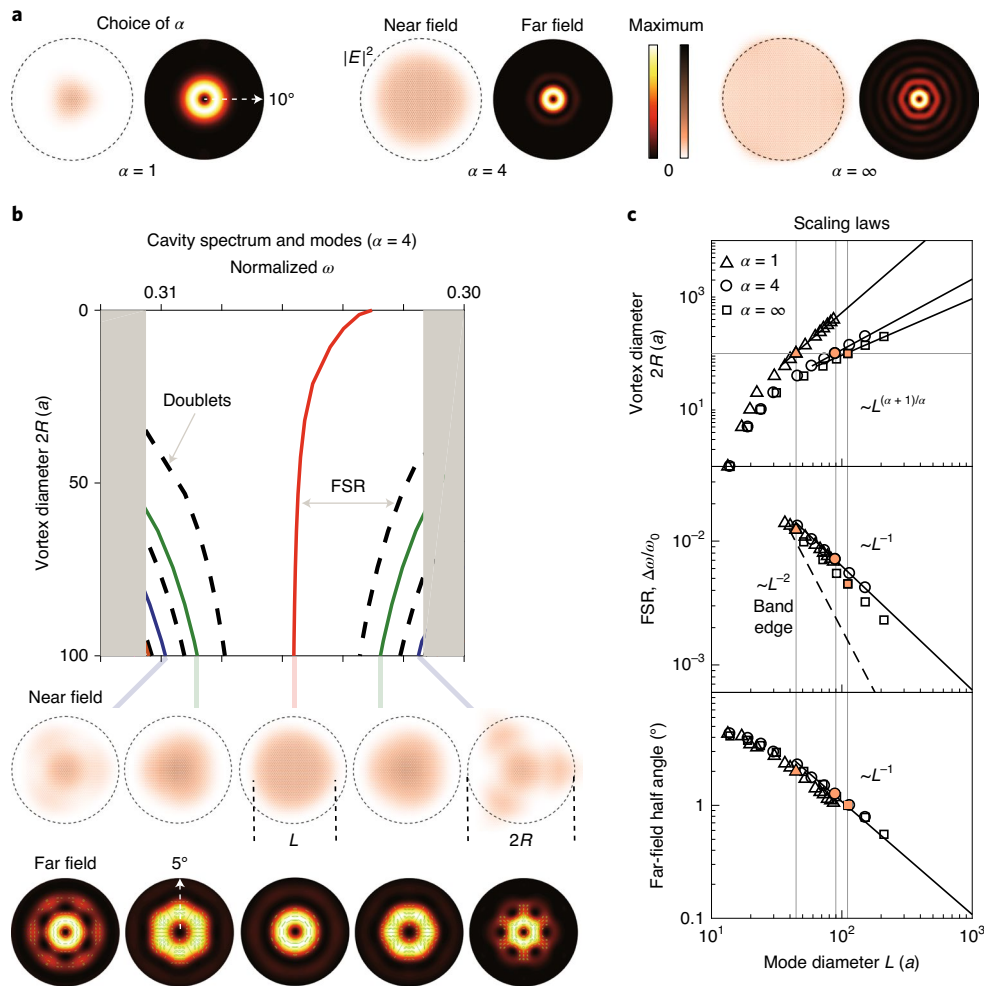


**Fig. 3 | Cavity properties as a function of the vortex size studied using 2D calculations with the effective refractive index 2.6.** **a**, Comparison of the near and far fields for different  $\alpha$  with the same vortex diameter  $2R=100a$ . **b**, The cavity spectrum and mode profiles. **c**, At the large mode limit, the mode diameter ( $L$ ) scales as  $R^{\alpha+1}$ ; the FSR scales as  $L^{-1}$ ; the far-field angle scales as  $L^{-1}$ . The colour-filled data points are from the three cavities in Fig. 3a. The FSR is computed as the frequency difference ( $\Delta\omega$ ) over the frequency of the topological mode ( $\omega_0$ ). When computing  $L$ , the boundary of the mode is defined at the outer edge where the field intensity drops to  $1/e$  of the central maximum intensity.

be very different from the size of the confined topological mode. For example, in Fig. 2f, the mode size is non-zero when  $R=0a$ , where  $a$  is the lattice constant. As shown in Fig. 3a, the mode size increases with  $\alpha$  for the same non-zero  $2R$ .

The fourth parameter  $\alpha$  is the shape factor—a positive exponent that controls the shape of the Dirac potential well (Fig. 2e);  $\alpha$  equal to 1, 2, 3 or 4 means a linear, quadratic, cubic or quartic well, respectively. When  $\alpha \rightarrow \infty$ ,  $\tanh(x^\infty)$  becomes a square well, inside which is the uniform unmodulated Dirac lattice ( $m_0=0$ ). In this case, the vertical radiation only takes place at the periphery of the well, resulting in a far-field pattern of many fringes (Fig. 3a) undesired for input–output coupling. (The  $Q$  and  $V$  dependence on  $\alpha$  is plotted in Supplementary Part F.) Considering both the radiative pattern and the mode area, a choice of  $\alpha=4$  is made in the following studies.

### Scaling laws

The Dirac-vortex cavity is continuously scalable in area by varying the vortex size  $2R$ . In Fig. 3, we examine numerically how the mode diameter, FSR and far-field angle scale with the vortex size ( $2R$ ). We set  $w=+1$  for single mode and choose a large band gap ( $m_0=0.1a$ ) for large FSRs.

A typical cavity spectrum is shown in Fig. 3b. For small cavities, the topological mode does not appear exactly at the gap centre, due

to the lack of exact chiral symmetry. (Fortunately, almost constant cavity frequencies, for all vortex sizes, can be realized by tuning the air-hole sizes at the cavity centre, as shown in Supplementary Part G.) For large cavities, the topological mode always converges to the Dirac-point frequency, since the central area of the large cavity approaches the unmodulated Dirac lattice with the original Dirac spectrum. As  $R$  increases, the high-order cavity modes originate from the continuum of bulk modes above or below the band gap. These high-order modes have both doublet and singlet states, due to the  $C_{3v}$  symmetry. The near fields and far fields of the singlet modes are plotted in Fig. 3b. The details of all modes are tabulated in Supplementary Part H. Compared to the high-order modes, the topological mode has the most extended mode area.

The modal diameter ( $L$ ) increases with the vortex diameter ( $2R$ ). The scaling is  $L \propto R^{\alpha+1}$  for large  $R$ , as shown in Fig. 3c. This is derived from the known result<sup>13</sup> that the zero-mode wavefunction  $\Psi_0(r)$  is determined by the radial integration of the mass function:  $|\Psi_0(r)| \propto e^{-\int_0^r |m(r')| dr'} \propto e^{-\int_0^r (r'/R)^\alpha dr'} \propto e^{-\frac{r^{\alpha+1}}{R^\alpha}}$ , according to the mass definition in equation (2). The size of the topological mode grows sub-linearly with  $R$  for finite  $\alpha$ . When  $\alpha=4$ ,  $L \propto R^5$  is close to a linear relation.

We numerically verify that the scaling law of FSR ( $\propto \frac{1}{\sqrt{V}} \propto \frac{1}{L}$ ) of the Dirac-vortex cavity is inversely proportional to the square

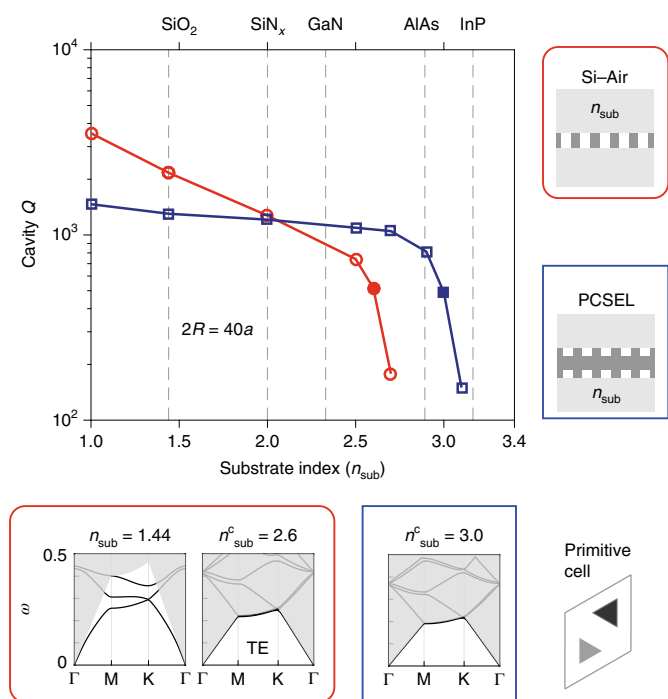


**Fig. 4 | Cavity  $Q$  as a function of substrate index ( $n_{\text{sub}}$ ) studied by 3D finite-difference-time-domain method for two configurations.** The central photonic-crystal waveguides are made of high-index material ( $n = 3.4$ ) and air. The  $Q$  spoils once  $n_{\text{sub}} > n_{\text{sub}}^c$ , when the Dirac point enters the light cone shaded in the band structures of the original honeycomb primitive cell. Both configurations have a limited vortex size of  $2R = 40a$  ( $\alpha = 4$ ) and are top-down symmetric to save computation resources.

root of the mode volume  $V$  and inversely proportional to the mode diameter  $L$ . As denoted in Fig. 3b, the FSR of the Dirac-vortex cavity is the frequency separation between the mid-gap and the neighbouring (doublet) modes. As plotted in Fig. 3c, the FSR of any  $\alpha$  values conforms to the same scaling law. It has been pointed out<sup>26</sup> that the FSR at a Dirac point (scales as  $L^{-1}$ ) can be much larger than the FSR of the usual quadratic band edge (scales as  $L^{-2}$ ). However, the proposed accidental ‘Dirac point’ at  $\Gamma$  in a previous study<sup>26</sup> is sensitive to the system parameters such as the air-hole size. In addition, the central flat band, in this three-fold accidental degeneracy, complicates the photonic states there. These problems are not present in the Dirac-vortex cavity.

The far-field half angle is inversely proportional to the mode diameter, as plotted in Fig. 3c. The beam angle is below  $1^\circ$  once the vortex diameter exceeds  $200a$ . Shown in Fig. 3a,b, the far fields of the singlet modes are vector beams, obtained by integrating the near fields ( $E_{x,y}$ ) using the Rayleigh–Sommerfeld diffraction theory. The polarization states of the vector beams are plotted with green lines at the bottom of Fig. 3b. Since the free-space polarization-degenerate modes belong to the doublet representation of  $C_{3v}$ , the singlet cavity modes cannot couple out in the exact vertical direction due to the distinct representations. If the  $C_{3v}$  symmetry is broken, one can convert the doughnut beam to a single-lobe beam<sup>38</sup>. We show such an example by non-uniform winding of the vortex in Supplementary Part I.

### Substrate compatibility

Substrate compatibility is crucial for device applications due to the practical requirements of heat dissipation, current conduction and mechanical support. In Fig. 4, we show that the Dirac-vortex cavities can work on various substrates. We place the cavity on uniform substrates and compute the  $Q$  as a function of substrate refractive index ( $n_{\text{sub}}$ ) for two different core waveguide

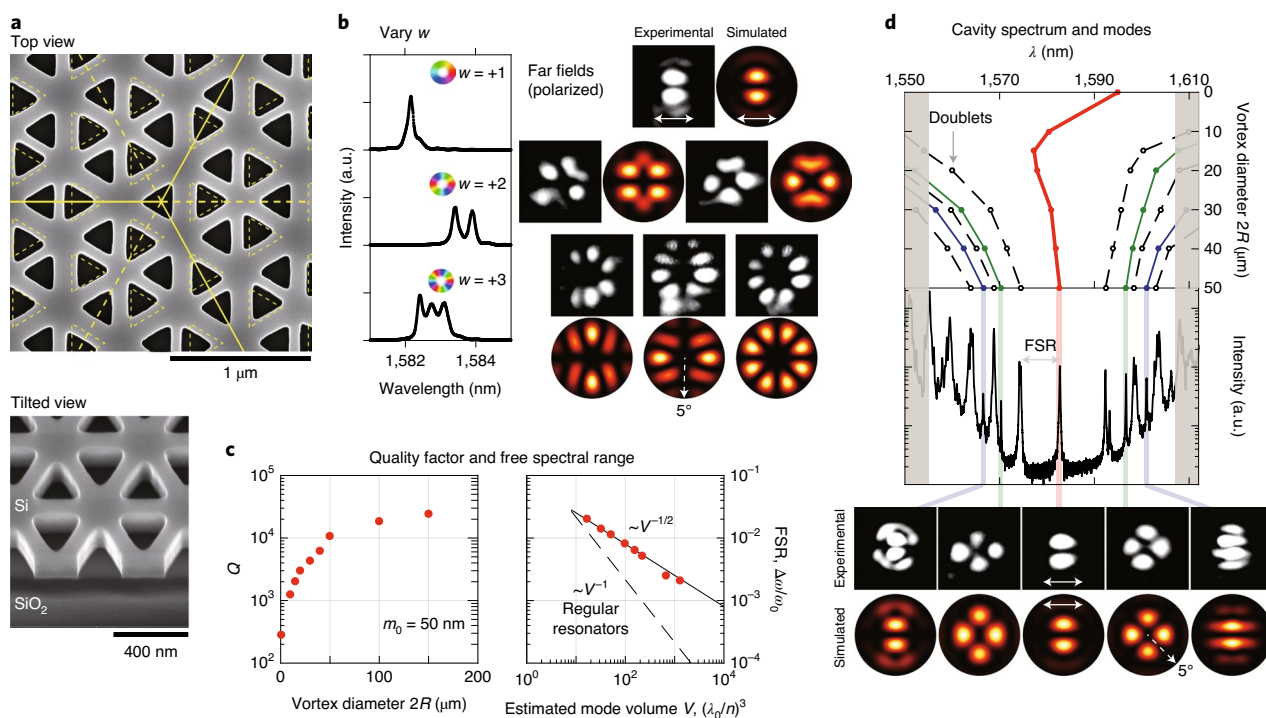


**Fig. 5 | Experimental studies of silica-cladded Dirac-vortex cavities with  $\alpha = 4$ ,  $m_0 = 50 \text{ nm}$  and  $a = 490 \text{ nm}$ .** **a**, Scanning electron microscope images of a cavity with  $R = 0 \mu\text{m}$  ( $0a$ ) and  $w = +1$ . The yellow lines illustrate the  $C_{3v}$  symmetry and the relative shifts of air holes. **b**, Optical spectra and far fields of cavity modes of different winding numbers with  $2R = 50 \mu\text{m}$  ( $100a$ ). **c**, The  $Q$  and FSR values of the single-vortex ( $w = +1$ ) cavities measured as a function of the vortex size  $R$  and the estimated mode volume  $V$ . **d**, The cavity spectrum as a function of vortex size. The far fields of five singlet modes are imaged and compared with simulations.

configurations: Si-air and PCSEL. Both high-index core waveguides are patterned with air.

In the Si-air configuration, we place the silicon membrane studied in Fig. 2 on the substrates. The cavity  $Q$  gradually decreases with increasing  $n_{\text{sub}}$  until a critical index value  $n_{\text{sub}}^c = 2.6$ , where  $Q$  drops off. This critical point is where the Dirac-point states, in the unperturbed primitive cell, are no longer guided in the core waveguide. The critical band structure is shown in Fig. 4, where the Dirac points almost merge into the light cones. This  $n_{\text{sub}}^c$  value already covers the common substrates such as silica, sapphire<sup>39</sup> and gallium nitride<sup>40</sup>.

In the PCSEL configuration, we aim to further increase  $n_{\text{sub}}^c$  and estimate the potential of the Dirac-vortex PCSELS. The PCSEL waveguide is twice as thick as the Si-air waveguide with the air-hole pattern through half of its total thickness from top and bottom. This structure is similar to the current PCSEL devices containing air holes<sup>8</sup>. The results in Fig. 4 show  $n_{\text{sub}}^c = 3.0$  and the band structures in Supplementary Part J show  $n_{\text{sub}}^c = 3.3$  for the all-semiconductor design<sup>41</sup>. These high  $n_{\text{sub}}^c$  values indicate the possible compatibility with the mature semiconductor material systems. The topological resonance persists even when the Dirac point is no longer frequency isolated. When the mode area is large enough, the wavevectors of the mode are too localized (in momentum space) to couple to the other bulk states of distinct momenta at the same frequency.

### Silicon-on-insulator experiments

We fabricate the Dirac-vortex cavities on silicon-on-insulator at telecommunication wavelength. The scanning electron microscope images of a typical device are shown in Fig. 5a. The photonic crystals were patterned in a 220 nm silicon layer by electron-beam lithography and dry-etching. The underneath SiO<sub>2</sub> cladding ensures mechanical stability. The cavity  $Q$  of asymmetric claddings (silica and air) sits in between the  $Q$  values of symmetric (both silica or both air) claddings in Fig. 4.

In Fig. 5b, cavities of different winding numbers ( $w = +1, +2, +3$ ) are measured. Their spectra verify that the number of topological modes equals the winding number. The far fields of all six modes compare favourably with the numerical results. The simulated near fields are listed in Supplementary Part K. These radiation patterns are captured after a horizontal polarizer in our cross-polarization set-up, illustrated in Supplementary Part L. The number of zero-intensity radial lines equals the topological charges (in magnitude) of these vector beams.

In Fig. 5c, we plot the dependence of  $Q$  and FSR on the cavity size. The  $Q$  increases with the increase of mode area and saturates between  $10^4$  and  $10^5$ , limited by fabrication imperfections. (The data of varying the maximum modulation amplitude  $m_0$  are plotted in Supplementary Part M.) The FSR is plotted as a function of the estimated mode volume ( $V$ ) according to numerical results in Fig. 3. The FSR of  $V^{-1/2}$  scaling is much larger than that of the  $V^{-1}$  scaling (dashed line) of regular cavities. For example, the experimental FSR is 8.22 nm for a 50  $\mu\text{m}$  Dirac-vortex cavity in Fig. 5d, while the FSR of a Fabry-Perot cavity with the same mode volume is only 1.28 nm, computed in Supplementary Part B.

In Fig. 5d, we plot the cavity resonances as a function of the vortex diameter. Consistent with the numerical results in Fig. 3b, the wavelength of the topological mode converges to the Dirac wavelength when the vortex diameter increases to about 30  $\mu\text{m}$ . We also track the high-order modes and a full spectrum is plotted for the cavity of  $2R = 50 \mu\text{m}$  (100a). The polarized far fields of the singlet modes are imaged and are in agreement with the numerical results. The far fields of all modes are tabulated in Supplementary Part H.

### Conclusions

Topological photonics<sup>15–17</sup> enabled us to design an on-chip optical microcavity<sup>42</sup> with separate controls over mode number ( $w$ ), mode area ( $R$ ), radiation coupling ( $m_0$ ) and scaling property ( $\alpha$ ).

The Dirac-vortex cavity is the 2D upgrade of the 1D feedback structures in phase-shifted DFBs and VCSELS, the two most widely used industrial single-mode semiconductor lasers. This topological resonator provides a single mid-gap mode with a large modal diameter continuously tunable from a few micrometres towards one millimetre, during which the FSR remains the largest among all known resonators.

The Dirac-vortex cavities offer a number of exciting opportunities. (1) They can be readily integrated with topological waveguides<sup>43–47</sup> to explore the potential of a topological photonic circuitry. (2) They provide a new method for on-chip vector-beam generation. (3) They are new types of degenerate cavities whose modal degeneracy is due to topology rather than ray optics<sup>48</sup>. (4) They can be used to construct topological PCSELS, by changing the lithography pattern, in the same semiconductor platform as that of the current PCSELS<sup>7–9,40,49</sup>, for a stabler single-mode operation, which generally implies higher yield, wider tuning range, narrower linewidth and greater output power.

### Online content

Any methods, additional references, Nature Research reporting summaries, source data, extended data, supplementary information, acknowledgements, peer review information; details of author contributions and competing interests; and statements of data and code availability are available at <https://doi.org/10.1038/s41565-020-0773-7>.

Received: 17 March 2020; Accepted: 28 August 2020;

Published online: 19 October 2020

### References

- Chuang, S. L. *Physics of Photonic Devices* (John Wiley and Sons, 2009).
- Kogelnik, H. & Shank, C. Stimulated emission in a periodic structure. *Appl. Phys. Lett.* **18**, 152–154 (1971).
- Haus, H. & Shank, C. Antisymmetric taper of distributed feedback lasers. *IEEE J. Quantum Electron.* **12**, 532–539 (1976).
- Sekartedjo, K. et al. 1.5  $\mu\text{m}$  phase-shifted dfb lasers for single-mode operation. *Electron. Lett.* **20**, 80–81 (1984).
- Wang, S. & Sheem, S. Two-dimensional distributed-feedback lasers and their applications. *Appl. Phys. Lett.* **22**, 460–462 (1973).
- Imada, M. et al. Coherent two-dimensional lasing action in surface-emitting laser with triangular-lattice photonic crystal structure. *Appl. Phys. Lett.* **75**, 316–318 (1999).
- Photonic crystal surface emitting laser diode L13395-04. *Hamamatsu Photonics* <https://www.hamamatsu.com/jp/en/product/lasers/semiconductor-lasers/pcsel/> (2018).
- Hirose, K. et al. Watt-class high-power, high-beam-quality photonic-crystal lasers. *Nat. Photon.* **8**, 406–411 (2014).
- Yoshida, M. et al. Double-lattice photonic-crystal resonators enabling high-brightness semiconductor lasers with symmetric narrow-divergence beams. *Nat. Mater.* **18**, 121–128 (2019).
- Shockley, W. On the surface states associated with a periodic potential. *Phys. Rev.* **56**, 317–323 (1939).
- Jackiw, R. & Rebbi, C. Solitons with fermion number 1/2. *Phys. Rev. D* **13**, 3398–3409 (1976).
- Su, W., Schrieffer, J. & Heeger, A. J. Solitons in polyacetylene. *Phys. Rev. Lett.* **42**, 1698–1701 (1979).
- Jackiw, R. & Rossi, P. Zero modes of the vortex-fermion system. *Nucl. Phys. B* **190**, 681–691 (1981).
- Hou, C.-Y., Chamon, C. & Mudry, C. Electron fractionalization in two-dimensional graphenelike structures. *Phys. Rev. Lett.* **98**, 186809 (2007).
- Lu, L., Joannopoulos, J. D. & Soljačić, M. Topological photonics. *Nat. Photon.* **8**, 821–829 (2014).
- Khanikaev, A. B. & Shvets, G. Two-dimensional topological photonics. *Nat. Photon.* **11**, 763–773 (2017).
- Ozawa, T. et al. Topological photonics. *Rev. Mod. Phys.* **91**, 015006 (2019).
- Bahari, B. et al. Nonreciprocal lasing in topological cavities of arbitrary geometries. *Science* **358**, 636–640 (2017).
- Bandres, M. A. et al. Topological insulator laser: experiments. *Science* **359**, eaar4005 (2018).
- Zeng, Y. et al. Electrically pumped topological laser with valley edge modes. *Nature* **578**, 246–250 (2020).

21. Shao, Z.-K. et al. A high-performance topological bulk laser based on band-inversion-induced reflection. *Nat. Nanotechnol.* **15**, 67–72 (2020).
22. Noh, J. et al. Topological protection of photonic mid-gap defect modes. *Nat. Photon.* **12**, 408–415 (2018).
23. Ota, Y. et al. Photonic crystal nanocavity based on a topological corner state. *Optica* **6**, 786–789 (2019).
24. Mittal, S. et al. Photonic quadrupole topological phases. *Nat. Photon.* **13**, 692–696 (2019).
25. Zhang, W. et al. Low-threshold topological nanolasers based on second-order corner state. *Light Sci. Appl.* **9**, 109 (2020).
26. Chua, S.-L., Lu, L., Bravo-Abad, J., Joannopoulos, J. D. & Soljačić, M. Larger-area single-mode photonic crystal surface-emitting lasers enabled by an accidental Dirac point. *Opt. Lett.* **39**, 2072–2075 (2014).
27. Bravo-Abad, J., Joannopoulos, J. D. & Soljačić, M. Enabling single-mode behavior over large areas with photonic Dirac cones. *Proc. Natl Acad. Sci. USA* **109**, 9761–9765 (2012).
28. Lu, L., Gao, H. & Wang, Z. Topological one-way fiber of second Chern number. *Nat. Commun.* **9**, 5384 (2018).
29. Teo, J. C. & Kane, C. L. Topological defects and gapless modes in insulators and superconductors. *Phys. Rev. B* **82**, 115120 (2010).
30. Iadecola, T., Schuster, T. & Chamon, C. Non-Abelian braiding of light. *Phys. Rev. Lett.* **117**, 073901 (2016).
31. Menssen, A. J., Guan, J., Felce, D., Booth, M. J. & Walmsley, I. A. A photonic Majorana bound state. *Phys. Rev. Lett.* **125**, 117401 (2020) (2019).
32. Noh, J. et al. Braiding photonic topological zero modes. Preprint at <http://arXiv.org/abs/1907.03208> (2019).
33. Gao, P. et al. Majorana-like zero modes in Kekulé distorted sonic lattices. *Phys. Rev. Lett.* **123**, 196601 (2019).
34. Chen, C.-W. et al. Mechanical analogue of a Majorana bound state. *Adv. Mater.* **31**, 1904386 (2019).
35. Barik, S., Miyake, H., DeGottardi, W., Waks, E. & Hafezi, M. Two-dimensionally confined topological edge states in photonic crystals. *New J. Phys.* **18**, 113013 (2016).
36. Barik, S. et al. A topological quantum optics interface. *Science* **359**, 666–668 (2018).
37. Wu, L.-H. & Hu, X. Scheme for achieving a topological photonic crystal by using dielectric material. *Phys. Rev. Lett.* **114**, 223901 (2015).
38. Miyai, E. et al. Lasers producing tailored beams. *Nature* **441**, 946 (2006).
39. Lu, L. et al. Gain compression and thermal analysis of a sapphire-bonded photonic crystal microcavity laser. *IEEE Photon. Technol. Lett.* **21**, 1166–1168 (2009).
40. Matsubara, H. et al. GaN photonic-crystal surface-emitting laser at blue-violet wavelengths. *Science* **319**, 445–447 (2008).
41. Taylor, R., Ivanov, P., Li, G., Childs, D. & Hogg, R. Optimisation of photonic crystal coupling through waveguide design. *Opt. Quantum Electron.* **49**, 47 (2017).
42. Vahala, K. J. Optical microcavities. *Nature* **424**, 839–846 (2003).
43. Shalaev, M. I., Walasik, W., Tsukernik, A., Xu, Y. & Litchinitser, N. M. Robust topologically protected transport in photonic crystals at telecommunication wavelengths. *Nat. Nanotechnol.* **14**, 31–34 (2018).
44. He, X.-T. et al. A silicon-on-insulator slab for topological valley transport. *Nat. Commun.* **10**, 872 (2019).
45. Ma, J., Xi, X. & Sun, X. Topological photonic integrated circuits based on valley kink states. *Laser Photon. Rev.* **13**, 1900087 (2019).
46. Peng, S. et al. Probing the band structure of topological silicon photonic lattices in the visible spectrum. *Phys. Rev. Lett.* **122**, 117401 (2019).
47. Liu, W. et al. Z<sub>2</sub> photonic topological insulators in the visible wavelength range for robust nanoscale photonics. *Nano Lett.* **20**, 1329–1335 (2020).
48. Arnaud, J. Degenerate optical cavities. *Appl. Opt.* **8**, 189–196 (1969).
49. Colombelli, R. et al. Quantum cascade surface-emitting photonic crystal laser. *Science* **302**, 1374–1377 (2003).

**Publisher's note** Springer Nature remains neutral with regard to jurisdictional claims in published maps and institutional affiliations.

© The Author(s), under exclusive licence to Springer Nature Limited 2020

**Data availability**

All relevant data are available from the authors on reasonable request.

**Acknowledgements**

We thank L. Gan, Y. Liang and G. Li for helpful discussions. L.L. acknowledges his PhD advisor J. D. O'Brien (1969–2017) for his teaching of photonic crystal lasers. L.L. was supported by the National Key R&D Program of China (2017YFA0303800, 2016YFA0302400), the Natural Science Foundation of China (11721404), the Strategic Priority Research Program of the Chinese Academy of Sciences (XDB33000000) and the Beijing Natural Science Foundation (Z200008). F.B. was supported by NSFC under grant nos 11734009 and 11674181.

**Author contributions**

L.L. conceived and led the project and wrote the paper. X.G. performed the simulations with help from H.L. and L.Z.; L.Y. performed device fabrication and characterization.

Z.W. contributed to the analytical model. All authors discussed the results and commented on the manuscript.

**Competing interests**

The authors declare no competing interests.

**Additional information**

**Supplementary information** is available for this paper at <https://doi.org/10.1038/s41565-020-0773-7>.

**Correspondence and requests for materials** should be addressed to L.L.

**Reprints and permissions information** is available at [www.nature.com/reprints](http://www.nature.com/reprints).

**Peer review information** *Nature Nanotechnology* thanks Yidong Chong and the other, anonymous, reviewer(s) for their contribution to the peer review of this work.